Contents lists available at ScienceDirect

Neurocomputing

journal homepage: www.elsevier.com/locate/neucom

TSFE-ITFI: A Unified Framework for Simultaneous Segmentation and Classification of Breast Ultrasound Images

Libin Lan*, Minghui Li

College of Computer Science and Engineering, Chongqing University of Technology, Chongqing, China

ARTICLE INFO

Keywords:
Bidirectional task interaction
Breast ultrasound imaging
Mamba2
Multi-task learning

ABSTRACT

Breast ultrasound (BUS) imaging plays a crucial role in early tumor diagnosis; however, achieving accurate joint segmentation and classification remains challenging due to low contrast, speckle noise, and ambiguous lesion boundaries in BUS images. Existing multi-task learning methods typically employ a shared-encoder paradigm, which often lacks explicit mechanisms for task-specific representations and effective cross-task interaction. To address these limitations, we propose TSFE-ITFI, a unified multi-task framework leveraging Task-Specific Feature Enhancement and Inter-Task Feature Interaction mechanisms for simultaneous segmentation and classification of breast tumors in BUS images. The proposed TSFE-ITFI adopts three key ideas. First, it utilizes a Convolution-Mamba2 feature fusion block in the segmentation branch to efficiently model long-range dependencies and restore fine-grained local details without incurring substantial computational costs. Second, it introduces a multi-scale channel-spatial attention mechanism in the classification branch to adaptively enhance informative features and suppress noise, thereby improving classification performance. Third, a bidirectional task interaction module is introduced to enable dynamic, adaptive, and bidirectional feature refinement between branches, facilitating information sharing and collaborative optimization. Extensive experiments on two public BUS datasets demonstrate that TSFE-ITFI obtains consistent and competitive performance in both segmentation and classification tasks, highlighting its effectiveness for joint breast ultrasound image analysis. Our code is available at here.

1. Introduction

Breast cancer remains one of the most commonly diagnosed cancers and a leading cause of cancer-related death among women worldwide, and early detection is critical for improving prognosis and survival outcomes [1]. Breast ultrasound (BUS) imaging is widely used in screening and diagnostic practice due to its non-invasive, real-time, relatively low-cost, and free of ionizing radiation [2]. In clinical practice, accurate tumor segmentation facilitates lesion localization and morphological assessment, whereas tumor classification provides important diagnostic guidance for distinguishing benign from malignant lesions. Therefore, developing automated methods that can jointly perform segmentation and classification from BUS images is of significant clinical value. However, BUS image analysis remains challenging because of severe speckle noise, low lesion-to-background contrast, and indistinct lesion boundaries, which hinder reliable feature extraction. In addition, marked

*Corresponding author

Email addresses: `lanlbn@cqut.edu.cn` (Libin Lan), `minghui.li@stu.cqut.edu.cn` (Minghui Li)

variations in tumor size, shape, and internal appearance make it difficult to capture discriminative lesion cues across different spatial scales, thereby limiting model robustness.

Multi-task learning (MTL) has emerged as a promising paradigm in medical image analysis. In BUS imaging, segmentation and classification are inherently correlated, where segmentation provides lesion-aware spatial priors for classification, while classification captures high-level semantic information that may help refine segmentation results. Recent studies have shown that jointly optimizing these two tasks within a unified framework can improve feature learning and overall diagnostic performance [3, 4]. However, existing BUS multi-task learning methods remain limited by their architectural design. Most approaches adopt a shared-encoder paradigm with lightweight task-specific heads, lacking explicit mechanisms for task-specific representations and effective inter-task interactions. Consequently, features associated with one task may dominate shared representations, leading to suboptimal performance or even negative transfer. Moreover, inter-task interactions are often modeled in an implicit or unidirectional manner, making it difficult to selectively and adaptively regulate information flow between the segmentation and classification branches.

Modeling long-range dependencies is another key challenge in BUS image analysis. Convolutional neural networks are constrained by local receptive fields, making it difficult to capture global contextual information. While attention-based architectures can model long-range dependencies, their quadratic computational and memory costs often limit their feasibility for high-resolution medical images [5]. Recently, state space model (SSM)-based architectures, such as Mamba, have demonstrated strong capability in modeling long-range dependencies with linear computational complexity [6]. Mamba2 further improves efficiency and representation capability through structured state space duality, providing a promising alternative for global context modeling [7]. However, the potential of Mamba2 in multi-task medical image analysis remains insufficiently explored.

To address the previously mentioned challenges, in this paper, we propose **TSFE-ITFI**, a unified multi-task framework for simultaneous segmentation and classification of breast tumors from BUS images, which integrates Task-Specific Feature Enhancement and Inter-Task Feature Interaction mechanisms. TSFE-ITFI encompasses three novel components. First, a Convolution-Mamba2 feature fusion (CM2FF) block is integrated into the decoder, i.e., the segmentation branch, to efficiently model long-range dependencies with linear computational complexity. This design enhances global context representation without substantial computational overhead while simultaneously recovering fine-grained local details via convolution's inherent inductive bias. Second, a multi-scale channel-spatial attention (MSCSA) mechanism is incorporated into the classification branch to adaptively refine complementary multi-level features by emphasizing discriminative lesion cues and suppressing irrelevant noise, thereby improving classification performance. Third, a bidirectional task interaction (BTI) module is introduced to enable dynamic, adaptive, and bidirectional feature modulation between tasks, allowing task-specific features to be selectively refined through cross-task information exchange. The integration of these three components enables TSFE-ITFI to explicitly model task-specific representations and achieve effective inter-task interactions. Overall, this study makes the following major contributions:

- We propose TSFE-ITFI, a unified multi-task learning framework for simultaneous segmentation and classification of breast tumors from BUS images within a single end-to-end architecture. TSFE-ITFI explicitly models task-specific representations and realizes effective cross-task interaction through three core components: CM2FF, MSCSA, and BTI.
- We propose three key well-designed components: CM2FF, MSCSA, and BTI. Specifically, the CM2FF block captures long-range dependencies and recovers fine-grained local details with minimal computational and memory overhead. The MSCSA mechanism suppresses irrelevant features, thereby improving classification performance and supporting more stable predictions in BUS images. Finally, the BTI module enables dynamic, bidirectional feature modulation between the segmentation and classification tasks.
- We conduct extensive experiments on two publicly available BUS datasets to evaluate the performance of TSFE-ITFI. The experimental results demonstrate that it can effectively model task-specific representations and realize cross-task interaction, thereby consistently outperforming existing state-of-the-art multi-task learning methods across both tasks, achieving superior performance in quantitative metrics and qualitative visualizations.

The remainder of this paper is organized as follows. Section 2 delves into previous relevant work and its limitations. Section 3 details our model architecture and the innovations of our method. Section 4 describes the experimental settings. Section 5 presents the results on two public BUS datasets, including quantitative and qualitative results, together with an in-depth analysis of the findings, followed by ablation studies and computational efficiency analysis. Section 6 summarizes our findings, points out the limitations of the work, and indicates directions for future research.

2. Related Work

2.1. Breast Ultrasound Image Segmentation

Encoder-decoder convolutional networks have become the dominant paradigm in medical image segmentation. The seminal U-Net [8] establishes the foundational symmetric architecture with skip connections, inspiring numerous variants that further enhance feature representation. For instance, Attention U-Net [9] introduces attention gates to suppress irrelevant regions, while U-Net++ [10] employs nested skip pathways to bridge the semantic gap between encoder and decoder features. Additionally, architectures such as DeepLabV3+ [11]

and CPFNet [12] demonstrate that expanding the receptive field and aggregating multi-scale contextual information are critical for handling objects with significant scale variations.

Building upon the success of U-shaped architectures, recent studies have developed more dedicated architectures for BUS segmentation. GG-Net [13] enhances lesion-aware localization by explicitly modeling global contextual information. AAU-net [14] introduces adaptive attention to improve lesion boundary perception under noisy ultrasound conditions, while C-Net [15] adopts cascaded refinement to progressively improve segmentation quality. Subsequently, hybrid CNN-transformer and advanced attention-based architectures have further enriched BUS segmentation research. HAU-Net [16] integrates transformer blocks into a U-shaped framework to improve long-range dependency modeling while preserving local detail representation. CoAtUNet [17] further adopts a symmetric encoder-decoder architecture, combining convolutional local features and self-attention global modeling for BUS segmentation. AMS-PAN [18] incorporates pyramid attention and multi-scale feature extraction to enhance tumor perception across different receptive fields. EMGANet [19] further improves boundary delineation by integrating edge-aware multi-scale group-mix attention mechanisms. In addition, CAU-net [20] addresses BUS-specific challenges such as noise interference, small lesions, and blurred boundaries through a challenge-aware multi-branch design. More recently, BA-MRGU-Net [21] employs foreground-background aware modeling and multi-scale region guidance to suppress background artifacts and strengthen lesion-region perception. Beyond BUS-specific models, Mamba-based architectures have recently emerged as a promising direction for efficient long-range dependency modeling in medical image segmentation. U-Mamba [22] shows that hybrid CNN-SSM designs can jointly preserve local-detail extraction and global-context modeling, while VM-UNet [23] further demonstrates the feasibility of building U-shaped medical segmentation frameworks with Vision Mamba blocks as the core context-modeling unit.

Nevertheless, despite the emerging exploration of Mamba-based architectures, most existing BUS segmentation models still rely on convolutional or attention-based feature extraction, with limited ability to efficiently model long-range dependencies in high-resolution images. This limitation may compromise the accurate delineation of large lesions and reduce robustness in the presence of acoustic shadowing and heterogeneous internal textures.

2.2. Breast Ultrasound Image Classification

Breast tumor classification in BUS images aims to distinguish benign from malignant lesions, providing critical support for clinical decision-making. Unlike segmentation, which requires precise boundary delineation, classification relies more on extracting discriminative semantic features. However, this task remains challenging due to speckle noise, low contrast, artifact interference, intra-lesional texture heterogeneity, and subtle morphological variations [24].

To address these limitations and mitigate data scarcity while improving generalization, many studies have adopted transfer learning based on ImageNet-pretrained backbones. For instance, multiview transfer learning strategies have been explored for automated breast ultrasound classification [25], and more recent work has compared transfer learning with automatic architecture design for BUS lesion classification [26]. In addition, explainable and lesion-sensitive classification frameworks have been investigated to improve clinical interpretability and robustness. Saliency-based explanation methods have been used to visualize the decision process of BUS classifiers [27], while joint localization- and lesion-aware classification frameworks explicitly encourage the network to focus on tumor-relevant regions rather than irrelevant background structures [4].

Despite these advances, most BUS classification models are still developed independently of segmentation. Without explicit lesion localization priors, the classifier may be distracted by background tissues, acoustic shadowing, or imaging artifacts. This issue is particularly problematic in BUS images, where benign and malignant lesions may differ only in subtle local morphology. Recent work has therefore begun to incorporate segmentation-aware cues into classification models, showing that lesion-guided feature extraction can improve diagnostic discrimination [28]. These observations motivate the design of more robust classification heads that can exploit multi-scale lesion-aware priors while suppressing speckle noise and ultrasound artifacts.

2.3. Multi-task Learning in BUS Image Analysis

Multi-task learning (MTL) has been extensively investigated in medical image analysis to jointly optimize correlated tasks within a unified architecture. In BUS imaging, segmentation and classification are inherently complementary. Specifically, segmentation provides lesion-aware spatial priors that guide the classification branch to focus on lesion-specific features, while classification contributes high-level semantic cues that facilitate segmentation refinement, particularly along indistinct boundaries. Therefore, integrating these tasks into an end-to-end framework has the potential to enhance task-specific representations and achieve more robust performance than using single-task counterparts.

Recent studies in BUS imaging have provided direct evidence for the effectiveness of joint learning. He et al. [3] propose a unified multi-task framework for simultaneous segmentation and classification of breast tumors from ultrasound images, showing that shared learning can improve both tasks. Fan et al. [4] demonstrate that joint localization and classification can enhance lesion-aware diagnosis in breast ultrasound imaging. Related work [28] has also shown that segmentation information can be explicitly integrated into classification pipelines, further supporting the value of lesion-aware feature sharing across tasks. More recently, CTEF-UNet [29] jointly models segmentation, classification, and edge detection through multi-scale fusion, cross-task attention, and edge-aware refinement, improving boundary precision and reducing false positives.

From a broader MTL perspective, early approaches often rely on hard parameter sharing and manually tuned loss weights [30]. To mitigate task interference, classical optimization strategies such as uncertainty-based loss weighting [31] and gradient normalization [32] have been proposed to balance the contributions of different tasks during training. Beyond loss balancing, architectural interaction mechanisms have attracted growing attention. For example, UML [33] enhances task collaboration through uncertainty-guided mutual learning, while MTAN [34] introduces task-specific soft-attention modules over a shared encoder-decoder network, and MTANet [35] adopts a shared transformer-based backbone with region-aware attention for segmentation enhancement. Lightweight attention modules such as CBAM [36] and channel recalibration strategies such as SENet [37] have also been widely adopted to refine shared representations. However, although recent methods have begun to explore more explicit cross-task guidance, many BUS multi-task frameworks still rely on shared backbones with implicit fusion or limited directional interaction, making it difficult to preserve task-specific discrimination while enabling effective collaboration.

Therefore, although existing multi-task BUS models have demonstrated the potential of joint optimization, how to achieve effective information sharing while maintaining task-specific discriminative features under noisy ultrasound conditions remains an open challenge. This limitation provides the motivation for our framework design.

2.4. Efficient Long-Range Dependency Modeling

Beyond task interaction, another important challenge in BUS analysis is how to effectively model long-range dependencies and global contextual information. While Transformer-based architectures have successfully addressed the local receptive field limitations of CNNs via self-attention [5], their quadratic computational complexity creates bottlenecks for high-resolution medical image analysis.

To overcome this limitation, modern deep state space models (SSMs) leverage discretized continuous-time systems to enable efficient sequence representation and computation. Among them, the structured state space sequence model (S4) [38] introduces a structured parameterization that improves the efficiency of long-range dependency modeling while preserving the principled state-space formulation. Mamba [6] further introduces a selective scan mechanism that adaptively propagates or filters information according to the input, thereby improving computational efficiency while maintaining effective context modeling. More recently, Mamba2 [7] further simplifies this framework through structured state space duality (SSD), leading to a simpler and more hardware-efficient selective SSM framework. Beyond the Mamba-based segmentation models discussed, MT-Mamba [39] explicitly combines self-task Mamba and cross-task Mamba blocks to jointly model long-range dependencies and cross-task interaction in dense prediction. However, the applicability of Mamba and its variants to multi-task breast ultrasound analysis, particularly for jointly addressing tumor segmentation and classification, remains underexplored and merits systematic investigation.

3. Method

3.1. Overall Framework

Fig. 1 illustrates the proposed TSFE-ITFI, a unified framework for simultaneous breast tumor segmentation and classification from BUS images. The architecture follows an encoder–decoder paradigm with a shared backbone. We employ a pre-trained ResNet-18 [40] as the encoder to extract hierarchical feature representations across four stages. Specifically, TSFE-ITFI comprises three core components: CM2FF, MSCSA, and BTI. First, the Convolution-Mamba2 feature fusion (CM2FF) block is integrated into the decoder, leveraging parallel convolutional and Mamba2 branches for hierarchical feature fusion. This design enables the decoder to efficiently capture fine local details and long-range contextual dependencies. Second, the multi-scale channel-spatial attention (MSCSA) mechanism is employed within a classification head to aggregate and refine multi-level features, thereby enhancing lesion-relevant representations and suppressing irrelevant background information. Finally, the bidirectional task interaction (BTI) module is positioned between the shared encoder and task-specific branches to facilitate explicit, adaptive, and gated information exchange between the segmentation and classification tasks.

3.2. Convolution-Mamba2 Feature Fusion Block

To effectively recover fine spatial details while incorporating global contextual information, we design a Convolution-Mamba2 feature fusion (CM2FF) block as the fundamental building unit in the first three decoder stages. As illustrated in Fig. 1, each CM2FF block comprises parallel convolutional (ConvM) and Mamba2 (Mamba2M) modules, followed by a summation fusion operation. Formally, the CM2FF operation is defined as:

$$\mathrm{CM2FF}(\boldsymbol{X}_i) = \mathrm{ConvM}(\boldsymbol{X}_i) + \mathrm{Mamba2M}(\boldsymbol{X}_i), i = 1, 2, 3, \quad (1)$$

where $\boldsymbol{X}_i \in \mathbb{R}^{C_i \times H_i \times W_i}$ represents the input feature map at the i-th decoder stage. This operation fuses convolutional and Mamba2 features via element-wise summation of the outputs from both ConvM and Mamba2M branches.

The ConvM captures local spatial details and employs two stacked 3×3 convolutional layers, followed by group normalization [41] and ReLU activation. In parallel, the Mamba2M models long-range contextual dependencies. Since Mamba2 operates on sequential tokens rather than 2D feature maps, the input feature $\boldsymbol{X}_i \in \mathbb{R}^{C_i \times H_i \times W_i}$ is first flattened along the spatial dimensions and then transposed into a token sequence, where each spatial location is treated as one token and the channel dimension serves as the token embedding dimension. The transformation can be written as:

$$\boldsymbol{X}_i^{\mathrm{seq}} = \mathrm{Trans}(\mathrm{Flatten}(\boldsymbol{X}_i)). \quad (2)$$

The resulting token sequence $\boldsymbol{X}_i^{\mathrm{seq}} \in \mathbb{R}^{H_i W_i \times C_i}$ is then processed by Mamba2 to capture long-range contextual dependencies

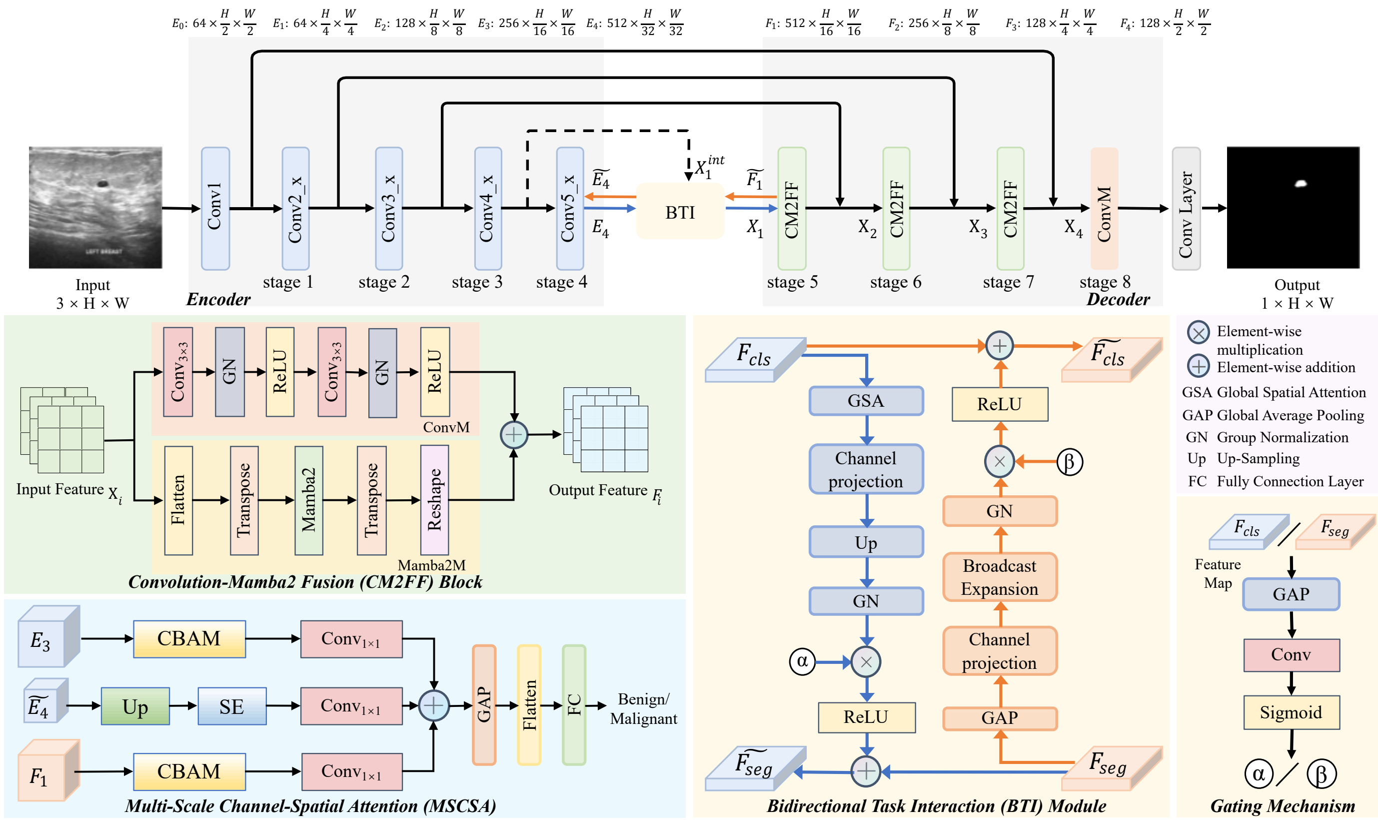

Fig. 1: Overall architecture of the proposed TSFE-ITFI. The network adopts an encoder–decoder framework with a shared ResNet-18 backbone. In the decoder, the first three stages employ Convolution-Mamba2 feature fusion (CM2FF) blocks for local-detail extraction and long-range dependency modeling, while the last stage uses convolution-only refinement for details recovery. A bidirectional task interaction (BTI) module explicitly models cross-task collaboration via adaptive, gated information exchange (α and β) between the classification and segmentation branches. The multi-scale channel-spatial attention (MSCSA) mechanism is employed within a classification head to aggregate the intermediate encoder feature $\boldsymbol{E}_3$, the BTI-updated high-level semantic feature $\widetilde{\boldsymbol{E}}_4$, and the first-stage decoder feature $\boldsymbol{F}_1$ using CBAM and SE blocks, thereby improving classification performance and supporting more stable predictions in BUS images. The segmentation branch produces pixel-wise tumor masks, while the classification branch outputs benign/malignant predictions in an end-to-end multi-task learning framework.

across spatial locations. After sequence modeling, the output is transposed back and reshaped to the original 2D feature maps:

$$\text{Mamba2M}(\boldsymbol{X}_i) = \text{Reshape}(\text{Trans}(\text{Mamba2}(\boldsymbol{X}_i^{\text{seq}}))). \tag{3}$$

The decoder comprises a four-stage hierarchical structure, employing CM2FF blocks in the first three stages and ConvM modules in the final stage. Initially, for the first decoder stage, the high-level encoder feature $\boldsymbol{E}_4$ is upsampled and concatenated with the corresponding encoder feature $\boldsymbol{E}_3$ to form an initial fusion feature $\boldsymbol{X}_1^{\text{int}}$. This intermediate representation, together with $\boldsymbol{E}_4$, is then fed into the bidirectional task interaction (BTI) module. The output of the BTI module subsequently serves as the actual input to the first fusion stage:

$$\boldsymbol{X}_1^{\text{int}} = \text{Cat}(\text{Up}(\boldsymbol{E}_4), \boldsymbol{E}_3), \tag{4}$$

$$(\widetilde{\boldsymbol{E}}_4, \boldsymbol{X}_1) = \text{BTI}(\boldsymbol{E}_4, \boldsymbol{X}_1^{\text{int}} or \widetilde{\boldsymbol{F}}_1), \tag{5}$$

$$\boldsymbol{F}_1 = \text{CM2FF}(\boldsymbol{X}_1), \tag{6}$$

where $\widetilde{\boldsymbol{F}}_1$ is the output $\boldsymbol{F}_1$ of CM2FF from the previous iteration. The second and third decoder stages are formulated as:

$$\boldsymbol{X}_2 = \text{Cat}(\text{Up}(\boldsymbol{F}_1), \boldsymbol{E}_2), \tag{7}$$

$$\boldsymbol{F}_2 = \text{CM2FF}(\boldsymbol{X}_2), \tag{8}$$

$$\boldsymbol{X}_3 = \text{Cat}(\text{Up}(\boldsymbol{F}_2), \boldsymbol{E}_1), \tag{9}$$

$$\boldsymbol{F}_3 = \text{CM2FF}(\boldsymbol{X}_3). \tag{10}$$

In this way, the first three CM2FF stages can jointly capture fine local details and global contextual information. In contrast to the preceding stages, the fourth stage incorporates only the ConvM module. Its input and corresponding output are defined as:

$$\boldsymbol{X}_4 = \text{Cat}(\text{Up}(\boldsymbol{F}_3), \boldsymbol{E}_0), \tag{11}$$

$$\boldsymbol{F}_4 = \text{ConvM}(\boldsymbol{X}_4). \tag{12}$$

This design choice is motivated by the fact that high-resolution feature maps in the final stage would generate prohibitively long token sequences, thereby imposing significant computational overhead on the Mamba2 module. Moreover, conventional convolutions are highly effective and efficient for local boundary refinement. Consequently, this design strategy achieves a favorable balance between contextual modeling capability and computational efficiency. Finally, the decoder's output $\boldsymbol{F}_4$ is used to predict the pixel-level segmentation mask via a 1×1 convolutional layer.

3.3. Multi-Scale Channel-Spatial Attention Mechanism

Breast ultrasound classification is highly sensitive to speckle noise, lesion scale variation, and ultrasound artifacts. To improve classification robustness under these conditions, we design a multi-scale channel-spatial attention (MSCSA) mechanism that aggregates features from different semantic and structural levels. Inspired by ACSNet [3], our classification head adopts a similar tripartite input structure, aggregating features from different semantic depths.

Specifically, the classification head takes three inputs: the intermediate encoder feature $\boldsymbol{E}_3$, the BTI-updated high-level classification feature $\widetilde{\boldsymbol{E}}_4$, and the refined feature $\boldsymbol{F}_1$ obtained from the first CM2FF stage. This input configuration is motivated by the complementary roles of the three feature levels. The intermediate encoder feature $\boldsymbol{E}_3$ preserves richer contextual and structural information, which is helpful for capturing lesion morphology. The BTI-updated high-level feature $\widetilde{\boldsymbol{E}}_4$ contains stronger semantic discrimination after receiving lesion-aware guidance through cross-task interaction. The refined feature $\boldsymbol{F}_1$ further incorporates decoder-side fusion and segmentation-enhanced lesion representations, making it more sensitive to tumor-relevant spatial details. By jointly leveraging these three inputs, the classification branch benefits from intermediate contextual cues, high-level object semantics, and decoder-enhanced lesion-aware features.

To adaptively refine the three feature streams, different attention modules are applied according to their representation characteristics. For $\boldsymbol{E}_3$ and $\boldsymbol{F}_1$, we employ the convolutional block attention module (CBAM) [36], since these two features retain more spatial details and are therefore more sensitive to local noise, lesion boundary variation, and irrelevant background structures. CBAM models channel and spatial attention in a sequential manner, making it suitable for refining spatially informative intermediate and decoder-enhanced features. For the BTI-updated high-level feature $\widetilde{\boldsymbol{E}}_4$, we adopt the squeeze-and-excitation (SE) block [37], which emphasizes channel-wise dependencies and is more appropriate for strengthening high-level semantic discrimination. Formally, the refined features are expressed as:

$$\boldsymbol{E}_3^{\mathrm{att}} = \mathrm{CBAM}(\boldsymbol{E}_3), \tag{13}$$

$$\widetilde{\boldsymbol{E}}_4^{\mathrm{att}} = \mathrm{SE}(\mathrm{Up}(\widetilde{\boldsymbol{E}}_4)), \tag{14}$$

$$\boldsymbol{F}_1^{\mathrm{att}} = \mathrm{CBAM}(\boldsymbol{F}_1). \tag{15}$$

To enable effective fusion, the refined features are first projected to a common channel dimension through 1×1 convolutions:

$$\widehat{\boldsymbol{E}}_3 = \mathrm{Conv}_{1\times1}(\boldsymbol{E}_3^{\mathrm{att}}), \tag{16}$$

$$\widehat{\boldsymbol{E}}_4 = \mathrm{Conv}_{1\times1}(\widetilde{\boldsymbol{E}}_4^{\mathrm{att}}), \tag{17}$$

$$\widehat{\boldsymbol{F}}_1 = \mathrm{Conv}_{1\times1}(\boldsymbol{F}_1^{\mathrm{att}}). \tag{18}$$

The fused representation is then obtained by:

$$\boldsymbol{F}_{\mathrm{fuse}} = \widehat{\boldsymbol{E}}_3 + \widehat{\boldsymbol{E}}_4 + \widehat{\boldsymbol{F}}_1. \tag{19}$$

Finally, the fused feature is aggregated by global average pooling and fed into a fully connected layer for classification:

$$z = \mathrm{Flatten}(\mathrm{GAP}(\boldsymbol{F}_{\mathrm{fuse}})),\ p = \mathrm{Softmax}(\boldsymbol{w}z + b), \tag{20}$$

where z denotes the pooled feature vector and p is the predicted probability distribution over the benign and malignant classes.

Compared with a single-scale classifier, the proposed MSCSA mechanism better aligns with the actual feature flow of the network by explicitly integrating intermediate encoder information, BTI-updated high-level object semantics, and decoder-refined lesion-aware representations. By combining multi-scale features with channel-spatial attention refinement, this design integrates complementary semantic, structural, and lesion-aware information across multiple feature levels, and enhances classification performance within the unified framework.

3.4. Bidirectional Task Interaction Module

To explicitly model cross-task interaction, we introduce a bidirectional task interaction (BTI) module that enables adaptive bidirectional feature modulation between the segmentation and classification branches via a gating mechanism. The architecture of the proposed bidirectional task interaction (BTI) module, including its gating mechanism, is illustrated in Fig. 1.

The BTI module employs asymmetric task-specific interaction strategies tailored to the distinct roles of the segmentation and classification branches. Specifically, the segmentation branch requires spatially aligned semantic guidance for pixel-level lesion delineation, whereas the classification branch benefits from compact lesion-aware global representations for image-level diagnosis. Accordingly, in the classification-to-segmentation path, classification features are refined by a global spatial attention (GSA) mechanism and projected into the segmentation feature space to preserve spatial localization cues. Conversely, in the segmentation-to-classification path, segmentation features are aggregated through global average pooling (GAP) and projected to provide compact global cues for classification. Therefore, the use of GSA and GAP is motivated by the different representational requirements of segmentation and classification, rather than by simply applying the same transformation to both interaction directions.

Let $\boldsymbol{F}_{\mathrm{cls}}$ and $\boldsymbol{F}_{\mathrm{seg}}$ denote the classification-side and segmentation-side features as BTI's inputs, respectively. We define two gating coefficients as:

$$\begin{aligned} \alpha &= \sigma(\mathrm{Conv}_{1\times1}(\mathrm{GAP}(\boldsymbol{F}_{\mathrm{cls}}))), \\ \beta &= \sigma(\mathrm{Conv}_{1\times1}(\mathrm{GAP}(\boldsymbol{F}_{\mathrm{seg}}))), \end{aligned} \tag{21}$$

where $\sigma(\cdot)$ denotes the sigmoid activation function. Here, α and β control the strength of cross-task feature modulation in the classification-to-segmentation and segmentation-to-classification directions, respectively.

For the classification-to-segmentation interaction, the transformed feature is defined as:

$$T_{\text{cls}\to\text{seg}}(\boldsymbol{F}_{\text{cls}}) = \text{Up}(\text{Proj}(\text{GSA}(\boldsymbol{F}_{\text{cls}}))), \tag{22}$$

where Proj($\cdot$) and Up($\cdot$) denote a 1×1 convolutional projection and using bilinear interpolation to match the spatial size of the segmentation branch, respectively. The updated segmentation feature is then computed as:

$$\widetilde{\boldsymbol{F}}_{\text{seg}} = \boldsymbol{F}_{\text{seg}} + \text{ReLU}(\alpha \otimes \text{Norm}(T_{\text{cls}\to\text{seg}}(\boldsymbol{F}_{\text{cls}}))), \tag{23}$$

where $\otimes$ denotes element-wise multiplication and Norm($\cdot$) denotes group normalization.

For the segmentation-to-classification interaction, the transformed feature is defined as:

$$T_{\text{seg}\to\text{cls}}(\boldsymbol{F}_{\text{seg}}) = \text{Exp}(\text{Conv}_{1\times1}(\text{GAP}(\boldsymbol{F}_{\text{seg}}))), \tag{24}$$

where Exp($\cdot$) denotes broadcasting the pooled feature to the spatial size of the classification branch. The updated classification feature is computed as:

$$\widetilde{\boldsymbol{F}}_{\text{cls}} = \boldsymbol{F}_{\text{cls}} + \text{ReLU}(\beta \otimes \text{Norm}(T_{\text{seg}\to\text{cls}}(\boldsymbol{F}_{\text{seg}}))). \tag{25}$$

In our implementation, the inputs to the BTI module are $\boldsymbol{F}_{\text{cls}} = \boldsymbol{E}_4$ and $\boldsymbol{F}_{\text{seg}} = \boldsymbol{X}_1^{\text{int}} or \widetilde{\boldsymbol{F}}_1$, and its outputs are denoted as $\widetilde{\boldsymbol{F}}_{\text{cls}} = \widetilde{\boldsymbol{E}}_4$ and $\widetilde{\boldsymbol{F}}_{\text{seg}} = \boldsymbol{X}_1$. The BTI operation can then be written as **Eq.** (5), where $\boldsymbol{X}_1$ is fed into the first CM2FF stage, while $\widetilde{\boldsymbol{E}}_4$ is used in the classification branch. Through this asymmetric yet complementary mechanism, the classification branch provides tumor-relevant semantic guidance to refine segmentation, while the segmentation branch supplies lesion-aware global contextual cues to enhance classification. In contrast to implicit feature sharing, the proposed BTI module enables a more explicit, dynamic, and task-adaptive approach to cross-task interaction.

3.5. Multi-task Loss Function

Following [42], we adopt a composite multi-task loss function to jointly optimize classification and segmentation tasks within a unified framework. The overall loss is defined as:

$$L_{\text{total}} = \lambda_{\text{cls}} L_{\text{cls}} + \lambda_{\text{ppa}} L_{\text{ppa}} + \lambda_{\text{lossnet}} L_{\text{lossnet}}, \tag{26}$$

where L_{cls} denotes the standard cross-entropy loss for classification, while L_{ppa} and L_{lossnet} represent the pixel position aware (PPA) loss [43] and the LossNet-based perceptual loss [44], respectively. The weighting coefficients λ_{cls}, λ_{ppa}, and $\lambda_{lossnet}$ balance the relative contributions of each objective during joint training.

By combining L_{ppa} and L_{lossnet}, the segmentation branch is supervised from both region-level overlap optimization and feature-level perceptual consistency, while L_{cls} encourages the classification branch to learn discriminative semantics.

4. Experimental Settings

4.1. Datasets

We evaluate TSFE-ITFI on two publicly available breast ultrasound (BUS) datasets: BUSI [45] and BUSI-WHU [19]. Both datasets offer pixel-level annotations for segmentation and image-level labels for classification, enabling rigorous evaluation of our multi-task framework. To ensure a fair and reliable estimate of generalization performance, three-fold cross-validation is independently conducted for each comparative method on both datasets. Final results are reported as the mean±standard deviation across the three folds.

4.1.1. BUSI

The BUSI dataset was collected from 600 female patients aged 25–75 years at the Baheya Hospital for Early Detection and Treatment of Women's Cancer in Cairo, Egypt. This collection consists of 780 ultrasound images acquired using LOGIQ E9 and LOGIQ E9 Agile systems and is categorized into three classes comprising 133 normal, 437 benign, and 210 malignant cases. All images are provided in PNG format with an average resolution of 500×500 pixels and include corresponding ground truth segmentation masks. The dataset is widely recognized for substantial intra-class variability, irregular tumor margins, and diverse morphological appearances, which render lesion delineation and malignancy discrimination particularly challenging. As our multi-task learning framework is designed to jointly segment and classify benign and malignant breast lesions, normal images are excluded from the dataset.

4.1.2. BUSI-WHU

The BUSI-WHU dataset was collected from patients aged 17 to 79 years who had been diagnosed with breast lesions. This collection comprises 927 breast ultrasound images, including 560 benign and 367 malignant samples, acquired using an ESAOTE LA523 ultrasound probe and a Mindray DC ultrasound system. Each image contains expert-annotated tumor regions. The dataset exhibits substantial diversity in tumor area and morphological characteristics, with notable variations in contrast, brightness, and boundary clarity. These imaging characteristics pose significant challenges for accurate boundary delineation and necessitate robust multi-scale feature representations.

4.2. Evaluation Metrics

To comprehensively evaluate the performance of the proposed TSFE-ITFI, we adopt a suite of metrics across all datasets [3, 19]. For segmentation, we report the Dice coefficient, Jaccard index, 95th percentile Hausdorff Distance (HD95), and Average Symmetric Surface Distance (ASD). For classification, we report Accuracy (ACC), Precision (PRE), Recall (REC), and F1-score. Additionally, we report floating-point operations (FLOPs), the number of parameters (#Params), and frames per second (FPS) to provide a comprehensive comparison in terms of computational complexity, model size, and inference efficiency. Finally, statistical significance is evaluated using metric-specific paired analyses: paired t-tests with p-values for per-image segmentation metrics and paired bootstrap analysis with 95% confidence intervals for classification metrics.

4.3. Implementation Details

All experiments are conducted using the PyTorch 2.3 framework on a single NVIDIA GeForce RTX 3090 GPU. TSFE-ITFI and all its variants are optimized using the Adam optimizer with the following settings: 100 epochs, an initial learning rate of $1e-4$, a weight decay of $1e-4$, and a batch size of 4. To adaptively adjust the learning rate during training, a LambdaLR scheduler is employed with decay parameters $\gamma = 0.2$ and $\lambda = 0.3$. The loss weighting coefficients are dataset-specific: for BUSI, we set $\lambda_{cls} = 0.5$, $\lambda_{ppa} = 1.0$, and $\lambda_{lossnet} = 0.1$; for BUSI-WHU, these are adjusted to $\lambda_{cls} = 0.6$, $\lambda_{ppa} = 0.9$, and $\lambda_{lossnet} = 0.1$.

All images and corresponding segmentation masks are resized to 256×256 pixels to standardize the receptive field coverage across samples. To enhance data diversity and improve model robustness, we apply morphology-preserving geometric augmentations, including random horizontal and vertical flipping as well as random rotation. These transformations simulate clinically relevant variations in tumor orientation and ultrasound probe positioning, thereby increasing spatial diversity without altering underlying pathological structures. As a result, the model achieves better generalization under heterogeneous ultrasound acquisition conditions.

5. Experimental Results

5.1. Comparisons with other state-of-the-art methods

We select several representative state-of-the-art single-task and multi-task methods for comparison with our TSFE-ITFI. The single-task baselines include nnU-Net [46], TransUNet [47], U-Mamba [22], and VM-UNet [23] for the segmentation task, as well as ResNet-18 [40] and MedMamba [48] for the classification task. The multi-task methods involve Deep U-Net [49], UML [33], CTEF-UNet [29], MTAN [34], MTANet [35], and ACSNet [3]. All methods are evaluated on the BUSI [45] and BUSI-WHU [19] datasets.

5.1.1. Comparison on BUSI

Quantitative Results. The quantitative comparison between TSFE-ITFI and representative single-task and multi-task methods on the BUSI dataset is presented in Table 1. One can see that TSFE-ITFI achieves the best overall performance across both segmentation and classification tasks. This improvement can be attributed to its explicit task-specific representations and bidirectional feature interaction within a unified framework.

For segmentation, TSFE-ITFI achieves state-of-the-art performance, yielding a Dice score of 82.88% and a Jaccard index of 75.98%, while also attaining the lowest boundary errors with HD95 of 14.14 mm and ASD of 4.19 mm. Compared to the second-best results, achieved by MTANet (Dice, HD95, ASD) and UML (Jaccard), our method improves Dice and Jaccard by 0.58% and 0.78%, respectively, and reduces HD95 and ASD by 0.98 mm and 0.49 mm. These improvements can be attributed to the synergistic effects of the CM2FF block and BTI module. The CM2FF block enhances long-range contextual modeling while recovering fine-grained details, which are critical for precise boundary delineation under challenging conditions such as low contrast and speckle noise. Meanwhile, the BTI module explicitly models cross-task interaction, enabling dynamic, adaptive, and bidirectional feature refinement between segmentation and classification tasks. In contrast, while UML [33] pioneers uncertainty-guided interaction, its feature modulation relies on uncertainty-derived weighting and operates primarily at high semantic levels, limiting its ability to refine fine-grained spatial details. Similarly, although MTANet [35] incorporates branch-specific designs that yield competitive segmentation performance, its cross-task collaboration remains implicit, relying mainly on shared backbone features and joint optimization rather than explicit interaction mechanisms. By explicitly modeling task-specific enhancements and cross-task interactions, TSFE-ITFI provides more accurate lesion characterization and boundary delineation in BUS images.

For classification, TSFE-ITFI also achieves state-of-the-art performance, attaining an accuracy of 94.59%, precision of 94.66%, recall of 93.84%, and F1-score of 94.59%. Compared to the second-best results, achieved by ACSNet (ACC, PRE, F1) and ResNet-18 (REC), surpassing the second-best baselines by 1.35–1.44 percentage points across all metrics. We attribute these gains to two key architectural advantages: MSCSA and BTI modules. The MSCSA aggregates intermediate encoder features $\boldsymbol{E}_3$, updated high-level features $\widetilde{\boldsymbol{E}}_4$, and decoder-refined features $\boldsymbol{F}_1$, applying tailored attention operations to each representation. Complementarily, the BTI module integrates lesion-aware cues from the segmentation branch into the classification pathway. These components enable TSFE-ITFI to effectively suppress background interference and capture more discriminative lesion characteristics. In contrast, while ACSNet [3] achieves competitive performance by aggregating multi-scale features, its classification relies primarily on channel attention to fuse shared features without explicitly differentiating the distinct semantic properties of different feature levels. Similarly, although ResNet-18 [40] leverages deep semantic representations beneficial for classification, as a single-task framework, it lacks access to the lesion-aware spatial information provided by the segmentation task.

Qualitative Results. Qualitative segmentation results of several prominent methods on the BUSI dataset are presented in Fig. 2. Compared to existing approaches, TSFE-ITFI produces segmentation masks that better align with the ground truth, exhibiting more complete lesion coverage, reduced fragmentation, and more accurate boundary delineation, particularly in cases with irregular shapes or ambiguous margins. These visual observations corroborate the quantitative metrics reported in Table 1, demonstrating the effectiveness of the proposed framework in improving breast tumor segmentation in BUS images.

5.1.2. Comparison on BUSI-WHU

Quantitative Results. Quantitative comparisons of different methods on the BUSI-WHU dataset are summarized in Table 2. TSFE-ITFI consistently achieves state-of-the-art performance across all evaluated segmentation and classification met-

Table 1: Quantitative results (mean$_{\pm\text{std}}$) of our approach against other state-of-the-art methods on the BUSI dataset. The symbol ↑ indicates the larger the better. The symbol ↓ indicates the smaller the better. The best result is in **bold**, and the second-best is underlined. Statistical significance is assessed via metric-specific paired analyses: paired t-tests with p-values for per-image segmentation metrics and paired bootstrap with 95% confidence intervals for classification metrics.

Paradigm	Method	Segmentation				Classification			
		Dice (%) ↑	Jaccard (%) ↑	HD95 (mm) ↓	ASD (mm) ↓	ACC (%) ↑	PRE (%) ↑	REC (%) ↑	F1 (%) ↑
Single-Task	nnU-Net [46]	$77.03_{\pm 0.87}$	$69.03_{\pm 0.86}$	$29.44_{\pm 3.44}$	$11.65_{\pm 1.41}$	-	-	-	-
	TransUNet [47]	$80.56_{\pm 0.81}$	$72.23_{\pm 0.78}$	$15.34_{\pm 0.90}$	$5.34_{\pm 0.29}$	-	-	-	-
	U-Mamba [22]	$77.10_{\pm 0.59}$	$69.40_{\pm 0.43}$	$27.92_{\pm 0.74}$	$10.98_{\pm 1.15}$	-	-	-	-
	VM-UNet [23]	$81.77_{\pm 1.36}$	$73.80_{\pm 1.44}$	$15.16_{\pm 1.13}$	$5.23_{\pm 0.38}$	-	-	-	-
	ResNet-18 [40]	-	-	-	-	$92.89_{\pm 0.79}$	$93.28_{\pm 0.58}$	$\underline{92.40_{\pm 1.39}}$	$92.91_{\pm 0.78}$
	MedMamba [48]	-	-	-	-	$83.77_{\pm 0.97}$	$84.08_{\pm 1.09}$	$81.40_{\pm 2.41}$	$83.72_{\pm 1.11}$
Multi-Task	Deep U-Net [49]	$79.20_{\pm 1.81}$	$71.50_{\pm 1.56}$	$19.58_{\pm 0.61}$	$6.85_{\pm 0.48}$	$90.11_{\pm 0.86}$	$90.28_{\pm 0.68}$	$88.49_{\pm 0.45}$	$90.09_{\pm 0.75}$
	UML [33]	$82.07_{\pm 2.19}$	$\underline{75.20_{\pm 2.15}}$	$19.08_{\pm 2.02}$	$6.54_{\pm 1.77}$	$91.50_{\pm 1.55}$	$91.68_{\pm 1.55}$	$89.32_{\pm 1.56}$	$91.40_{\pm 1.57}$
	MTAN [34]	$77.67_{\pm 1.13}$	$68.83_{\pm 0.79}$	$19.22_{\pm 1.18}$	$7.23_{\pm 0.93}$	$92.74_{\pm 1.15}$	$92.84_{\pm 1.30}$	$91.94_{\pm 2.18}$	$92.75_{\pm 1.19}$
	MTANet [35]	$\underline{82.30_{\pm 1.77}}$	$75.13_{\pm 1.44}$	$\underline{15.12_{\pm 0.62}}$	$\underline{4.68_{\pm 0.60}}$	$92.42_{\pm 1.76}$	$92.52_{\pm 1.71}$	$91.18_{\pm 2.30}$	$92.40_{\pm 1.79}$
	ACSNet [3]	$81.97_{\pm 1.33}$	$74.77_{\pm 1.33}$	$18.93_{\pm 1.18}$	$6.33_{\pm 1.00}$	$\underline{93.20_{\pm 1.90}}$	$\underline{93.31_{\pm 1.89}}$	$91.78_{\pm 2.28}$	$\underline{93.18_{\pm 2.28}}$
	CTEF-UNet [29]	$77.82_{\pm 0.75}$	$68.70_{\pm 0.56}$	$17.98_{\pm 2.42}$	$6.16_{\pm 1.95}$	$91.66_{\pm 1.88}$	$91.89_{\pm 1.84}$	$90.59_{\pm 1.38}$	$91.68_{\pm 1.80}$
	TSFE-ITFI	$\mathbf{82.88_{\pm 1.24}}$	$\mathbf{75.98_{\pm 1.79}}$	$\mathbf{14.14_{\pm 1.16}}$	$\mathbf{4.19_{\pm 1.75}}$	$\mathbf{94.59_{\pm 1.19}}$	$\mathbf{94.66_{\pm 1.20}}$	$\mathbf{93.84_{\pm 1.43}}$	$\mathbf{94.59_{\pm 1.19}}$
p-value		3.321e-3	3.153e-3	6.900e-5	4.200e-5	-	-	-	-
95% confidence interval		-	-	-	-	[0.01, 3.09]	[0.10, 3.13]	[0.49, 4.13]	[0.06, 3.14]

Table 2: Quantitative results (mean$_{\pm\text{std}}$) of our approach against other state-of-the-art methods on the BUSI-WHU dataset. The symbol ↑ indicates the larger the better. The symbol ↓ indicates the smaller the better. The best result is in **bold**, and the second-best is underlined. Statistical significance is assessed via metric-specific paired analyses: paired t-tests with p-values for per-image segmentation metrics and paired bootstrap with 95% confidence intervals for classification metrics.

Paradigm	Method	Segmentation				Classification			
		Dice (%) ↑	Jaccard (%) ↑	HD95 (mm) ↓	ASD (mm) ↓	ACC (%) ↑	PRE (%) ↑	REC (%) ↑	F1 (%) ↑
Single-Task	nnU-Net [46]	$87.67_{\pm 0.31}$	$79.63_{\pm 0.48}$	$13.61_{\pm 1.10}$	$4.32_{\pm 0.63}$	-	-	-	-
	TransUnet [47]	$88.58_{\pm 0.51}$	$80.40_{\pm 0.63}$	$5.15_{\pm 1.31}$	$0.93_{\pm 0.40}$	-	-	-	-
	U-Mamba [22]	$88.00_{\pm 0.70}$	$80.20_{\pm 0.86}$	$12.41_{\pm 1.47}$	$3.98_{\pm 0.65}$	-	-	-	-
	VM-UNet [23]	$88.90_{\pm 0.18}$	$80.99_{\pm 0.08}$	$5.26_{\pm 1.33}$	$0.96_{\pm 0.06}$	-	-	-	-
	ResNet-18 [40]	-	-	-	-	$83.93_{\pm 0.61}$	$83.98_{\pm 0.48}$	$82.00_{\pm 1.11}$	$83.69_{\pm 0.69}$
	MedMamba [48]	-	-	-	-	$72.71_{\pm 1.07}$	$72.94_{\pm 1.03}$	$70.69_{\pm 0.90}$	$72.36_{\pm 1.17}$
Multi-Task	Deep U-Net [49]	$87.73_{\pm 0.68}$	$80.67_{\pm 0.76}$	$7.95_{\pm 0.97}$	$1.30_{\pm 0.21}$	$83.71_{\pm 1.50}$	$84.29_{\pm 1.45}$	$81.96_{\pm 2.71}$	$83.41_{\pm 1.75}$
	UML [33]	$89.83_{\pm 0.84}$	$82.93_{\pm 1.00}$	$6.58_{\pm 1.11}$	$1.23_{\pm 0.47}$	$82.53_{\pm 0.70}$	$82.63_{\pm 0.63}$	$81.05_{\pm 0.23}$	$82.38_{\pm 0.59}$
	MTAN [34]	$86.57_{\pm 0.54}$	$77.74_{\pm 0.74}$	$6.52_{\pm 1.18}$	$0.98_{\pm 0.40}$	$83.82_{\pm 1.21}$	$84.07_{\pm 1.38}$	$82.50_{\pm 0.44}$	$83.70_{\pm 1.03}$
	MTANet [35]	$\underline{90.10_{\pm 0.22}}$	$83.37_{\pm 0.05}$	$\underline{5.59_{\pm 0.29}}$	$0.98_{\pm 0.30}$	$83.82_{\pm 1.21}$	$83.85_{\pm 1.30}$	$82.37_{\pm 1.47}$	$83.70_{\pm 1.15}$
	ACSNet [3]	$89.93_{\pm 0.25}$	$\underline{83.43_{\pm 0.24}}$	$5.69_{\pm 0.40}$	$\underline{0.84_{\pm 0.11}}$	$83.82_{\pm 0.92}$	$83.75_{\pm 0.83}$	$82.28_{\pm 0.37}$	$83.68_{\pm 0.89}$
	CTEF-UNet [29]	$87.53_{\pm 0.16}$	$78.74_{\pm 0.24}$	$5.78_{\pm 0.07}$	$1.02_{\pm 0.09}$	$\underline{84.25_{\pm 1.50}}$	$\underline{84.33_{\pm 1.57}}$	$\underline{83.70_{\pm 1.36}}$	$\underline{84.28_{\pm 1.52}}$
	TSFE-ITFI	$\mathbf{90.33_{\pm 0.09}}$	$\mathbf{83.57_{\pm 0.29}}$	$\mathbf{4.51_{\pm 0.49}}$	$\mathbf{0.66_{\pm 0.16}}$	$\mathbf{84.79_{\pm 1.15}}$	$\mathbf{84.89_{\pm 1.21}}$	$\mathbf{83.85_{\pm 1.06}}$	$\mathbf{84.74_{\pm 1.17}}$
p-value		5.524e-3	7.985e-3	1.851e-2	1.082e-2	-	-	-	-
95% confidence interval		-	-	-	-	[0.03, 1.08]	[0.04, 1.12]	[0.01, 0.43]	[0.03, 0.94]

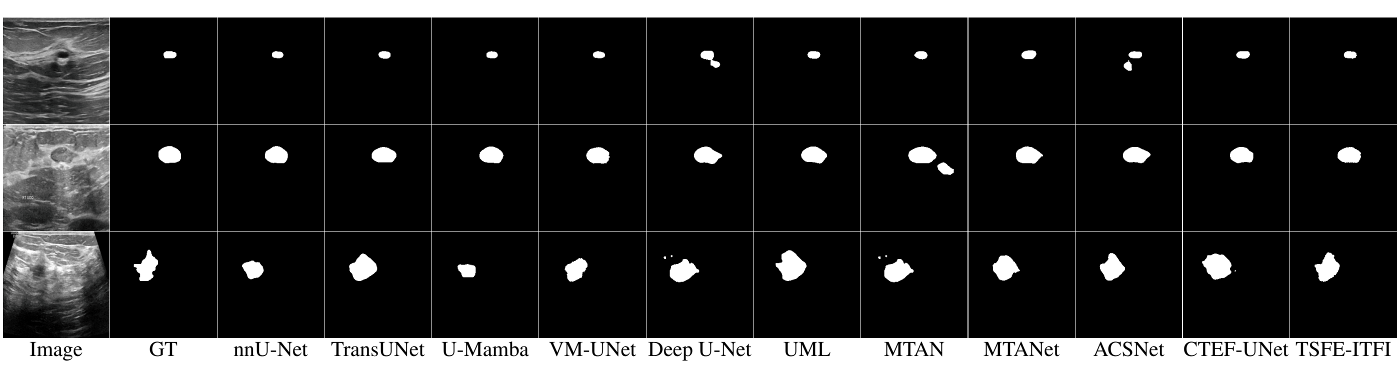

Fig. 2: Qualitative segmentation results of our approach against other state-of-the-art methods on the BUSI dataset. From left to right: input image, ground truth, and predictions from nnU-Net [46], TransUNet [47], U-Mamba [22], VM-UNet [23], Deep U-Net [49], UML [33], MTAN [34], MTANet [35], ACSNet [3], CTEF-UNet [29], and our proposed TSFE-ITFI. TSFE-ITFI produces segmentation masks with superior boundary delineation and more complete lesion coverage compared to most baselines, particularly in cases with low contrast or irregular shapes. Best viewed in color with zoom.

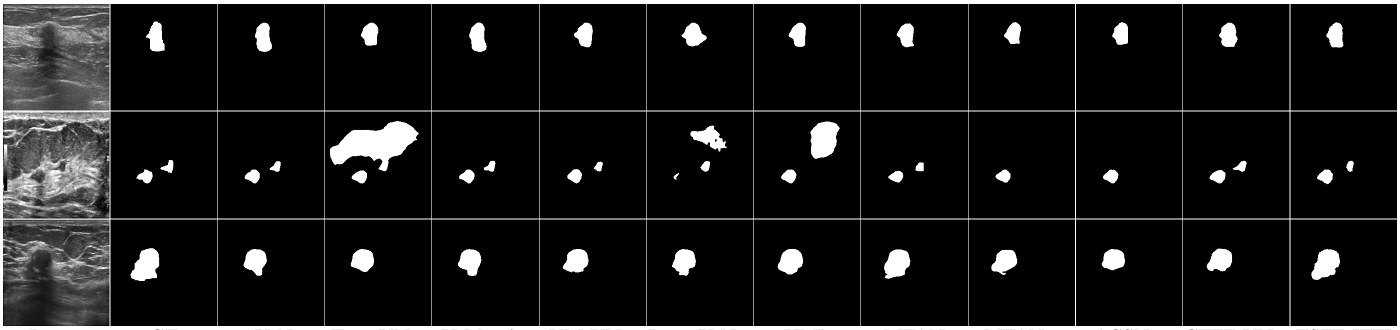

Fig. 3: Qualitative segmentation results of our approach against other state-of-the-art methods on the BUSI-WHU dataset. From left to right: input image, ground truth, and predictions from nnU-Net [46], TransUNet [47], U-Mamba [22], VM-UNet [23], Deep U-Net [49], UML [33], MTAN [34], MTANet [35], ACSNet [3],]CTEF-UNet [29], and TSFE-ITFI. The qualitative behavior of TSFE-ITFI on BUSI-WHU closely mirrors that observed on the BUSI dataset.

rics, showing that the proposed framework maintains competitive performance on diverse BUS benchmarks.

For segmentation, TSFE-ITFI achieves a Dice score of 90.33%, a Jaccard index of 83.57%, an HD95 of 4.51 mm, and an ASD of 0.66 mm. Compared to the second-best results, achieved by MTANet (Dice, HD95) and ACSNet (Jaccard, ASD), our method improves Dice and Jaccard by 0.23 and 0.14 percentage points, respectively, while reducing HD95 and ASD by 1.08 mm and 0.18 mm. For classification, TSFE-ITFI achieves an accuracy of 84.79%, precision of 84.89%, recall of 83.85%, and F1-score of 84.74%, surpassing the second-best baseline by 0.54, 0.56, 0.15, and 0.46 percentage points, respectively.

These improvements mirror the advantages observed on BUSI, further supporting the effectiveness of the proposed framework for joint segmentation and classification on the BUS datasets. We ascribe this performance advantage to our dedicated architectural choices, specifically the explicit learning of task-specific representations and the effective integration of cross-task interaction modules.

Qualitative Results. Qualitative segmentation results on the BUSI-WHU dataset are presented in Fig. 3. Compared to other methods, TSFE-ITFI produces segmentation masks with more accurate lesion delineation, particularly in challenging cases characterized by acoustic shadowing and blurred boundaries. These visual observations are consistent with the quantitative improvements reported in Table 2, further validating the robustness of the proposed framework across diverse BUS imaging protocols.

5.1.3. Significance Analysis

Although the absolute improvements on BUSI-WHU appear modest, e.g., +0.23% Dice and +0.14% Jaccard, we emphasize that statistical significance depends not only on mean differences but also on prediction variance and sample size. Accordingly, for segmentation metrics, we perform paired t-tests comparing TSFE-ITFI against the second-best method for each metric, using per-image paired metric values obtained from the same test samples, with $N = 647$ paired observations on BUSI and $N = 927$ paired observations on BUSI-WHU. For classification metrics, we employ paired bootstrap analysis to estimate the 95% confidence intervals for improvements in ACC, PRE, REC, and F1-score. All p-values yielded by the paired t-tests are below 0.05, and all confidence intervals derived by the bootstrap protocol exclude zero, indicating that the observed improvements are statistically significant despite small absolute gains.

5.2. Ablation Study

In this section, we conduct an extensive ablation study on the BUSI dataset to thoroughly evaluate the contribution of each key component in TSFE-ITFI. Specifically, we investigate the individual and combined effects of the CM2FF, MSCSA, and BTI modules. The ablation results for these components and their combinations are summarized in Table 3.

5.2.1. Effectiveness of CM2FF

The integration of only CM2FF into the baseline architecture leads to consistent segmentation gains: +0.27% in Dice, +0.06% in Jaccard, and reductions of 0.46 mm in HD95 and 0.86 mm in ASD. These improvements confirm our design hypothesis that jointly leveraging convolutional local feature extraction and Mamba2-based long-range modeling enables more robust spatial-contextual representations, ultimately improving boundary accuracy for irregular BUS lesions. Furthermore, this variant equipped solely with CM2FF exhibits a slight improvement in classification performance, suggesting that CM2FF provides lesion-aware spatial cues beneficial for classification. The contribution of CM2FF remains evident in the full framework. Removing CM2FF while retaining BTI and MSCSA reduces the Dice score by 0.75% and the Jaccard index by 0.68%, while HD95 and ASD increase by 4.13 mm and 1.98 mm, respectively. This performance degradation, particularly in boundary-sensitive metrics, indicates that CM2FF contributes to more accurate lesion delineation. Together, CM2FF plays a critical role in multi-task learning, particularly for segmentation, and works in concert with the other components to achieve robust joint optimization.

To systematically investigate the internal design of CM2FF, we conduct an ablation study on the BUSI dataset, comparing four configurations: ConvM-only, Mamba2M-only, concatenation-based fusion, and summation-based fusion. As summarized in Table 4, the single-branch variants yield comparable performance. Specifically, ConvM-only achieves a

Table 3: Ablation study on the impact of each component and their combinations within TSFE-ITFI on the BUSI dataset. The best result is highlighted in **bold**.

Components			Segmentation				Classification			
CM2FF	MSCSA	BTI	Dice (%) ↑	Jaccard (%) ↑	HD95 (mm) ↓	ASD (mm) ↓	ACC (%) ↑	PRE (%) ↑	REC (%) ↑	F1 (%) ↑
✗	✗	✗	$81.90_{\pm 0.93}$	$75.27_{\pm 1.13}$	$17.67_{\pm 1.07}$	$6.07_{\pm 0.07}$	$91.96_{\pm 1.16}$	$92.16_{\pm 1.08}$	$90.63_{\pm 1.68}$	$91.94_{\pm 1.16}$
✓	✗	✗	$82.17_{\pm 1.70}$	$75.33_{\pm 1.83}$	$17.21_{\pm 0.24}$	$5.21_{\pm 0.47}$	$92.43_{\pm 1.44}$	$92.53_{\pm 1.39}$	$91.63_{\pm 1.70}$	$92.45_{\pm 1.43}$
✗	✓	✗	$81.80_{\pm 1.81}$	$74.93_{\pm 2.32}$	$17.07_{\pm 1.25}$	$5.59_{\pm 0.63}$	$92.27_{\pm 2.19}$	$92.54_{\pm 2.18}$	$92.16_{\pm 2.60}$	$92.34_{\pm 2.18}$
✗	✗	✓	$82.10_{\pm 1.65}$	$75.37_{\pm 1.69}$	$17.35_{\pm 1.74}$	$5.58_{\pm 0.58}$	$92.12_{\pm 1.00}$	$92.27_{\pm 0.88}$	$91.50_{\pm 0.78}$	$92.16_{\pm 0.97}$
✓	✓	✗	$82.17_{\pm 1.52}$	$75.20_{\pm 1.71}$	$18.01_{\pm 1.30}$	$5.66_{\pm 0.94}$	$92.89_{\pm 1.76}$	$93.05_{\pm 1.68}$	$92.05_{\pm 2.24}$	$92.89_{\pm 1.77}$
✓	✗	✓	$82.50_{\pm 1.89}$	$75.60_{\pm 1.94}$	$18.88_{\pm 0.56}$	$5.59_{\pm 0.29}$	$93.02_{\pm 1.53}$	$93.08_{\pm 1.51}$	$91.41_{\pm 2.02}$	$92.94_{\pm 1.53}$
✗	✓	✓	$82.13_{\pm 1.25}$	$75.30_{\pm 1.61}$	$18.27_{\pm 1.53}$	$6.17_{\pm 0.58}$	$93.04_{\pm 1.66}$	$93.21_{\pm 1.61}$	$92.41_{\pm 2.07}$	$93.06_{\pm 1.67}$
✓	✓	✓	$\mathbf{82.88_{\pm 1.24}}$	$\mathbf{75.98_{\pm 1.79}}$	$\mathbf{14.14_{\pm 1.16}}$	$\mathbf{4.19_{\pm 1.75}}$	$\mathbf{94.59_{\pm 1.19}}$	$\mathbf{94.66_{\pm 1.20}}$	$\mathbf{93.84_{\pm 1.43}}$	$\mathbf{94.59_{\pm 1.19}}$

Table 4: Ablation study of CM2FF on the BUSI dataset. The symbol ↑ indicates the larger the better. The symbol ↓ denotes the smaller the better. The best result is in **bold**, and the second-best is underlined.

Components			Segmentation				Classification			
ConvM	Mamba2M	Fusion	Dice (%) ↑	Jaccard (%) ↑	HD95 (mm) ↓	ASD (mm) ↓	ACC (%) ↑	PRE (%) ↑	REC (%) ↑	F1 (%) ↑
✓	✗	–	$82.13_{\pm 1.25}$	$75.30_{\pm 1.61}$	$18.27_{\pm 1.53}$	$6.17_{\pm 0.58}$	$93.04_{\pm 1.66}$	$\underline{93.21_{\pm 1.61}}$	$\underline{92.41_{\pm 2.07}}$	$93.06_{\pm 1.19}$
✗	✓	–	$82.27_{\pm 2.31}$	$75.33_{\pm 2.57}$	$17.50_{\pm 0.55}$	$5.98_{\pm 0.99}$	$93.04_{\pm 2.31}$	$93.20_{\pm 2.29}$	$92.03_{\pm 2.06}$	$93.00_{\pm 2.35}$
✓	✓	Concat	$\underline{82.70_{\pm 2.14}}$	$\underline{75.53_{\pm 2.68}}$	$\underline{16.86_{\pm 2.32}}$	$\underline{5.70_{\pm 1.29}}$	$\underline{93.20_{\pm 1.17}}$	$93.16_{\pm 1.18}$	$92.14_{\pm 2.21}$	$\underline{93.15_{\pm 1.16}}$
✓	✓	Sum	$\mathbf{82.88_{\pm 1.24}}$	$\mathbf{75.98_{\pm 1.79}}$	$\mathbf{14.14_{\pm 1.16}}$	$\mathbf{4.19_{\pm 1.75}}$	$\mathbf{94.59_{\pm 1.19}}$	$\mathbf{94.66_{\pm 1.20}}$	$\mathbf{93.84_{\pm 1.43}}$	$\mathbf{94.59_{\pm 1.19}}$

Dice score of 82.13% and a Jaccard index of 75.30%, while Mamba2M-only attains 82.27% and 75.33%, respectively. These results confirm that both convolution-based local feature extraction and Mamba2-based long-range dependency modeling are beneficial for lesion segmentation. However, relying on a single branch proves suboptimal. Combining both branches via concatenation improves the Dice and Jaccard scores to 82.70% and 75.53%, respectively. Notably, the proposed summation fusion achieves the best overall performance, reaching 82.88% Dice, 75.98% Jaccard, 14.14 mm HD95, 4.19 mm ASD, and 94.59% F1. Compared to concatenation, summation reduces HD95 from 16.86 mm to 14.14 mm and ASD from 5.70 mm to 4.19 mm, indicating more precise and stable boundary delineation. These results indicate that summation fusion provides a more compact and effective way to integrate convolution-derived local details and Mamba2-based contextual information for lesion segmentation.

5.2.2. *Effectiveness of MSCSA*

Integrating MSCSA alone into the baseline architecture yields consistent classification gains: +0.31% in accuracy, +0.38% in precision, +1.53% in recall, and +0.40% in F1-score. However, compared to the baseline, this variant exhibits a slight decline in segmentation performance in terms of Dice and Jaccard. These results suggest that MSCSA primarily strengthens multi-scale discriminative representations for classification, while its individual contribution to segmentation is limited, potentially due to task interference. The effectiveness of MSCSA becomes more pronounced within the complete TSFE-ITFI framework. When integrated with CM2FF and BTI, MSCSA boosts classification performance by 1.57–2.43 percentage points across all metrics, while also yielding segmentation improvements. These findings validate that the explicit task-specific design of MSCSA effectively aggregates multi-scale features and supplies deep semantic representations, which, when combined with CM2FF and BTI, enable robust multi-task optimization.

To further evaluate the robustness of MSCSA, we directly test TSFE-ITFI models with and without MSCSA, trained on the original BUSI training set, against BUSI test images corrupted by three representative perturbations [46, 50]: speckle noise, contrast degradation, and background interference. We report the F1-score as the primary metric, as it balances precision and recall to provide a comprehensive assessment of classification stability under degraded conditions. First, synthetic speckle noise is simulated using multiplicative Gaussian perturbation with variance $\sigma \in \{0.1, 0.2, 0.3\}$, where higher values produce more pronounced speckle-like artifacts. Second, contrast degradation is induced via gamma correction with $\gamma \in \{0.5, 0.7, 1.5\}$; specifically, $\gamma < 1$ brightens low-intensity regions, while $\gamma > 1$ darkens the image and compresses low-intensity responses. Third, background perturbation is introduced by adding zero-centered Gaussian noise exclusively to non-lesion pixels, leaving the lesion region intact. The perturbation magnitude is controlled by the standard deviation δ, set to 0.2 and 0.5 in our experiments. As shown in Fig. 4, the full model with MSCSA consistently outperforms the variant without MSCSA across most perturbation settings, particularly under speckle noise and background perturbation. The smaller performance drop observed at the highest noise levels indicates that MSCSA enhances classification stability in noisy environments. Although its advantage diminishes under extreme contrast degradation ($\gamma = 1.5$), the full model still maintains F1 performance comparable to its ablated counterpart.

To investigate whether the three inputs of MSCSA are necessary, we conduct an input-selection ablation on the BUSI dataset. As shown in Table 5, the proposed $\boldsymbol{E}_3+\widetilde{\boldsymbol{E}}_4+\boldsymbol{F}_1$ design achieves the best overall classification performance, improving F1 from 92.94% to 94.59%. Using only the high-level feature $\widetilde{\boldsymbol{E}}_4$ already improves classification compared with the plain GAP+FC head, indicating the importance of semantic discrimination. Adding $\boldsymbol{E}_3$ further improves F1 to 94.04%, suggesting that intermediate structural and contextual cues are useful for benign/malignant discrimination. The $\widetilde{\boldsymbol{E}}_4 + \boldsymbol{F}_1$ variant also

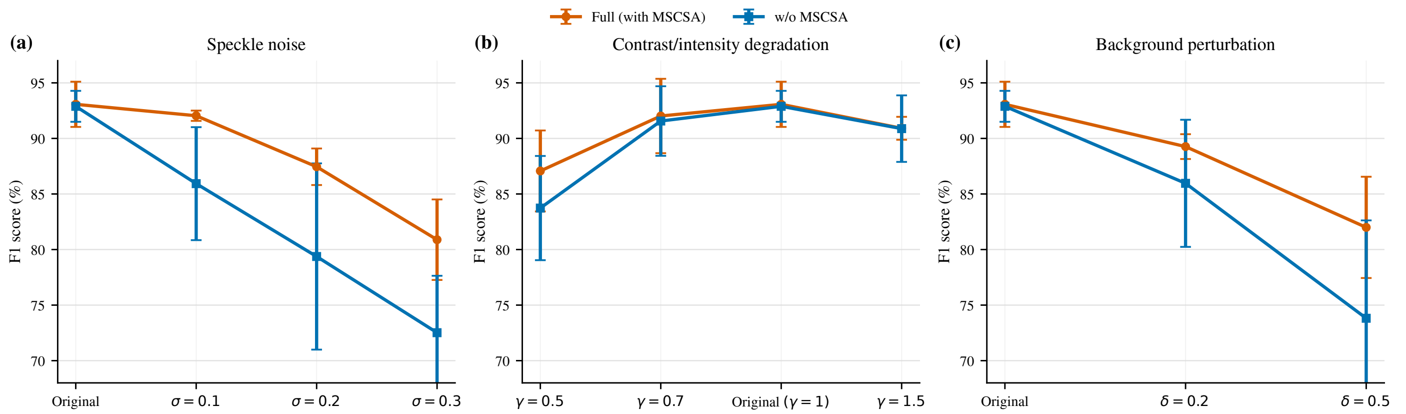

Fig. 4: Robustness evaluation of TSFE-ITFI with and without MSCSA under synthetic perturbations on the BUSI dataset. F1-scores are reported as mean ± standard deviation across three-fold cross-validation under varying levels of (a) multiplicative speckle noise σ, (b) contrast degradation via gamma correction γ, and (c) background perturbation δ. The full model with MSCSA consistently outperforms the ablated variant under most conditions, demonstrating enhanced stability against speckle noise and background interference, while maintaining comparable performance under extreme contrast degradation.

Table 5: Ablation study of different input feature combinations in MSCSA on the BUSI dataset. The symbol ↑ indicates the larger the better. The symbol ↓ denotes the smaller the better. The best result is in **bold**, and the second-best is underlined.

Variant	Segmentation				Classification			
	Dice (%) ↑	Jaccard (%) ↑	HD95 (mm) ↓	ASD (mm) ↓	ACC (%) ↑	PRE (%) ↑	REC (%) ↑	F1 (%) ↑
GAP+FC	$82.50_{\pm1.89}$	$75.60_{\pm1.94}$	$18.88_{\pm0.56}$	$5.59_{\pm0.29}$	$93.02_{\pm1.53}$	$93.08_{\pm1.51}$	$91.41_{\pm2.02}$	$92.94_{\pm1.53}$
$\widetilde{\boldsymbol{E}}_4$	$82.15_{\pm1.23}$	$75.54_{\pm1.31}$	$17.54_{\pm1.10}$	$5.88_{\pm0.64}$	$93.58_{\pm2.01}$	$93.61_{\pm2.04}$	$92.59_{\pm2.51}$	$93.58_{\pm2.03}$
$\boldsymbol{E}_3$+$\widetilde{\boldsymbol{E}}_4$	$82.03_{\pm1.75}$	$75.09_{\pm1.81}$	$17.80_{\pm1.18}$	$5.98_{\pm0.47}$	$94.04_{\pm1.74}$	$94.27_{\pm1.55}$	$93.06_{\pm1.89}$	$94.04_{\pm1.70}$
$\widetilde{\boldsymbol{E}}_4$+$\boldsymbol{F}_1$	$82.29_{\pm1.50}$	$75.55_{\pm1.72}$	$17.25_{\pm0.21}$	$5.47_{\pm0.38}$	$93.89_{\pm1.53}$	$94.02_{\pm1.47}$	$92.63_{\pm1.94}$	$93.87_{\pm1.52}$
$\boldsymbol{E}_3$+$\widetilde{\boldsymbol{E}}_4$+$\boldsymbol{F}_1$	$\mathbf{82.88_{\pm1.24}}$	$\mathbf{75.98_{\pm1.79}}$	$\mathbf{14.14_{\pm1.16}}$	$\mathbf{4.19_{\pm1.75}}$	$\mathbf{94.59_{\pm1.19}}$	$\mathbf{94.66_{\pm1.20}}$	$\mathbf{93.84_{\pm1.43}}$	$\mathbf{94.59_{\pm1.19}}$

outperforms the single-input design, indicating that decoder-refined lesion-aware features provide complementary information. These results indicate that the intermediate encoder context $\boldsymbol{E}_3$, BTI-updated high-level semantics $\widetilde{\boldsymbol{E}}_4$, and decoder-refined lesion-aware feature $\boldsymbol{F}_1$ provide complementary information rather than redundant information for classification.

5.2.3. Effectiveness of BTI

Integrating BTI alone into the baseline architecture yields consistent improvements across both segmentation and classification metrics. These results demonstrate that BTI facilitates effective cross-task feature interaction, mutually enhancing task performance. Within the full TSFE-ITFI framework, the integration of BTI with CM2FF and MSCSA boosts performance on both tasks by significant margins, particularly in boundary precision, where HD95 is reduced by 3.87 mm. These findings underscore BTI's capability to effectively leverage complementary information from both tasks, which is beneficial for joint optimization, especially for enhancing lesion boundary delineation under challenging BUS imaging conditions.

To further investigate the necessity of the directional interaction and gating mechanism in BTI, we decompose BTI into several controlled variants and evaluate them on the BUSI dataset. As shown in Table 6, all variants are implemented under the same framework with CM2FF and MSCSA enabled, and only the BTI interaction strategy is modified. The BTI variants show clear complementary effects. classification-to-segmentation interaction only improves segmentation over w/o BTI, increasing Dice from 82.17% to 82.60% and reducing HD95 from 18.01 mm to 16.61 mm, but slightly decreases classification F1. In contrast, segmentation-to-classification interaction only improves F1 from 92.89% to 93.26%, while slightly reducing Dice. These results suggest that classification-derived semantic features facilitate lesion delineation, whereas segmentation-side lesion-aware cues contribute to improved diagnostic classification. The ungated bidirectional variant improves segmentation but fails to improve classification, suggesting that unrestricted cross-task feature injection may introduce task interference. By contrast, the proposed BTI achieves the best overall performance, improving Dice, Jaccard, and F1 by 0.71%, 0.78%, and 1.70%, respectively, while reducing HD95 and ASD by 3.87 mm and 1.47 mm over w/o BTI. This validates the benefit of combining bidirectional interaction with adaptive gating. To further analyze adaptiveness, we record α and β for each test sample across all three folds. As shown in Table 7 and Fig. 5, both gates show clear sample-level variation rather than collapsing to constants. Moreover, β is generally higher than α, indicating that classification-to-segmentation interaction only provides stronger lesion-aware guidance for classification, while the non-zero and sample-varying α confirms that segmentation-to-classification interaction only still offers complementary semantic guidance for segmentation.

5.2.4. Effectiveness of Combinations

When all three components are integrated, the complete TSFE-ITFI achieves optimal performance across both tasks. For segmentation, the Dice score reaches 82.88%, the Jaccard index increases to 75.98%, and HD95 and ASD are reduced to

Table 6: Ablation study of BTI variants on the BUSI dataset. The symbol ↑ indicates the larger the better. The symbol ↓ denotes the smaller the better. The best result is in **bold**, and the second-best is underlined. cls→seg and seg→cls indicate the classification-to-segmentation and segmentation-to-classification interactions, respectively.

Variant	Segmentation				Classification			
	Dice (%) ↑	Jaccard (%) ↑	HD95 (mm) ↓	ASD (mm) ↓	ACC (%) ↑	PRE (%) ↑	REC (%) ↑	F1 (%) ↑
w/o BTI	$82.17_{\pm 1.52}$	$75.20_{\pm 1.71}$	$18.01_{\pm 1.30}$	$5.66_{\pm 0.94}$	$92.89_{\pm 1.76}$	$93.05_{\pm 1.68}$	$92.05_{\pm 2.24}$	$92.89_{\pm 1.77}$
cls→seg only	$82.60_{\pm 1.52}$	$75.65_{\pm 1.75}$	$16.10_{\pm 1.70}$	$5.37_{\pm 0.48}$	$92.27_{\pm 0.96}$	$92.53_{\pm 0.48}$	$91.46_{\pm 0.35}$	$92.30_{\pm 0.47}$
seg→cls only	$81.93_{\pm 1.52}$	$75.09_{\pm 1.56}$	$17.46_{\pm 0.46}$	$5.46_{\pm 0.56}$	$93.20_{\pm 2.08}$	$93.56_{\pm 1.86}$	$92.96_{\pm 2.11}$	$93.26_{\pm 2.00}$
ungated bidirectional	$82.50_{\pm 1.62}$	$75.66_{\pm 1.86}$	$16.99_{\pm 1.86}$	$5.70_{\pm 0.40}$	$92.73_{\pm 1.58}$	$92.97_{\pm 1.39}$	$91.60_{\pm 1.76}$	$92.72_{\pm 1.56}$
Proposed BTI	$\mathbf{82.88_{\pm 1.24}}$	$\mathbf{75.98_{\pm 1.79}}$	$\mathbf{14.14_{\pm 1.16}}$	$\mathbf{4.19_{\pm 1.75}}$	$\mathbf{94.59_{\pm 1.19}}$	$\mathbf{94.66_{\pm 1.20}}$	$\mathbf{93.84_{\pm 1.43}}$	$\mathbf{94.59_{\pm 1.19}}$

Table 7: Statistics of the learned gating coefficients across all test samples on the BUSI dataset.

Coefficient	Mean ± Std	Range	Benign mean ($n = 437$)	Malignant mean ($n = 210$)
α (cls → seg)	$0.227_{\pm 0.125}$	[0.050, 0.628]	0.208	0.266
β (seg → cls)	$0.783_{\pm 0.073}$	[0.594, 0.916]	0.812	0.723

14.14 mm and 4.19 mm, respectively, indicating more accurate lesion delineation. For classification, the full model attains an accuracy of 94.59%, precision of 94.66%, recall of 93.84%, and F1-score of 94.59%. Compared to the baseline, the complete model improves all classification metrics by 2.5–3.21 percentage points. These results demonstrate that CM2FF, MSCSA, and BTI are complementary, and their joint integration yields clear benefits for both segmentation and classification. Notably, variants combining any two of the three components also exhibit substantial gains over the baseline, further validating the effectiveness of TSFE-ITFI.

Table 8: Comparison of model complexity in terms of FLOPs, parameter counts, and inference speed. The FLOPs for segmentation are calculated with 256×256 input. All metrics are reported for the segmentation task. The symbol ↑ indicates the larger the better. The symbol ↓ indicates the smaller the better. The best result is in **bold**, and the second-best is underlined. Our result is highlighted in *italicized*.

Paradigm	Method	FLOPs (G) ↓	#Params (M) ↓	FPS (img/s) ↑
Single-Task	nnU-Net [46]	14.34	**20.62**	**248.78**
	TransUNet [47]	32.23	93.23	41.99
	U-Mamba [22]	24.39	28.76	123.94
	VM-UNet [23]	9.82	44.27	44.64
Multi-Task	Deep Unet [49]	7.79	26.50	180.36
	UML [33]	175.52	62.17	35.17
	MTAN [34]	54.73	51.74	122.59
	MTANet [35]	**7.65**	29.71	33.82
	ACSNet [3]	27.05	32.65	55.49
	CTEF-UNet [29]	17.26	75.86	64.42
	TSFE-ITFI	*19.66*	*22.56*	*64.10*

5.3. Computational Efficiency Analysis

We further evaluate computational efficiency in terms of FLOPs, parameter count (#Params), and inference speed (FPS), as summarized in Table 8. FLOPs are computed using a 256×256 input image, and FPS is measured under identical hardware configurations to ensure fair comparison across methods. All metrics are evaluated for the segmentation task.

5.3.1. Efficiency Analysis of Single-Task Approaches

Among the single-task methods, nnU-Net achieves the highest inference speed at 248.78 FPS while maintaining relatively low complexity, with 14.34G FLOPs and 20.62M parameters. This efficiency could be attributed to its purely convolutional and self-configuring architecture. In contrast, TransUNet exhibits higher complexity, requiring 32.23G FLOPs and 93.23M parameters, and achieves only 41.99 FPS. This is likely because it models long-range dependencies through self-attention mechanisms, which incur quadratic computational and memory costs. U-Mamba, a hybrid CNN-SSM architecture, attains 123.94 FPS with 24.39G FLOPs and 28.76M parameters, demonstrating that state space models can offer a favorable balance between representational capacity and computational efficiency.

5.3.2. Efficiency Analysis of Multi-Task Approaches

Among multi-task approaches, Deep U-Net, an early method employing a shared encoder with task-specific decoders, achieves notably low computational cost with 7.79G FLOPs and 26.50M parameters and high inference speed of 180.36 FPS. However, as shown in Tables 1 and 2, its relatively simple architecture limits segmentation performance. MTAN facilitates cross-task interaction via task-specific soft-attention modules at multiple encoder-decoder levels; while this enhances feature interaction, it increases complexity to 54.73G FLOPs, 51.74M parameters, and 122.59 FPS. UML is the most computationally expensive method, requiring 175.52G FLOPs and 62.17M parameters while achieving only 35.17 FPS. This high cost can be attributable to its structurally complex mutual-learning pipeline. CTEF-UNet, a closely related BUS multi-task baseline, requires 17.26G FLOPs and 75.86M parameters and achieves 64.42 FPS. Its relatively large parameter count may be partly due to its edge-guided refinement, cross-task attention, and multi-level dense fusion design. ACSNet introduces gating units at skip connections alongside DSA modules in the decoder to improve feature selection and deformation-aware segmentation, resulting in 27.05G FLOPs, 32.65M parameters, and 55.49 FPS. Finally, despite low complexity with 7.65G FLOPs and 29.71M parameters, MTANet achieves only 33.82 FPS, indicating that memory-sensitive operations, rather than FLOPs alone, determine practical inference efficiency.

In contrast to prior approaches, TSFE-ITFI achieves efficient multi-task learning via a lightweight shared ResNet-18 backbone coupled with a CM2FF-enhanced decoder. This hybrid architecture integrates convolutional local feature extraction with Mamba2-based long-range modeling, balancing high representational power, achieving best performance as shown in Tables 1 and 2, with modest computational cost, with 19.66G FLOPs,

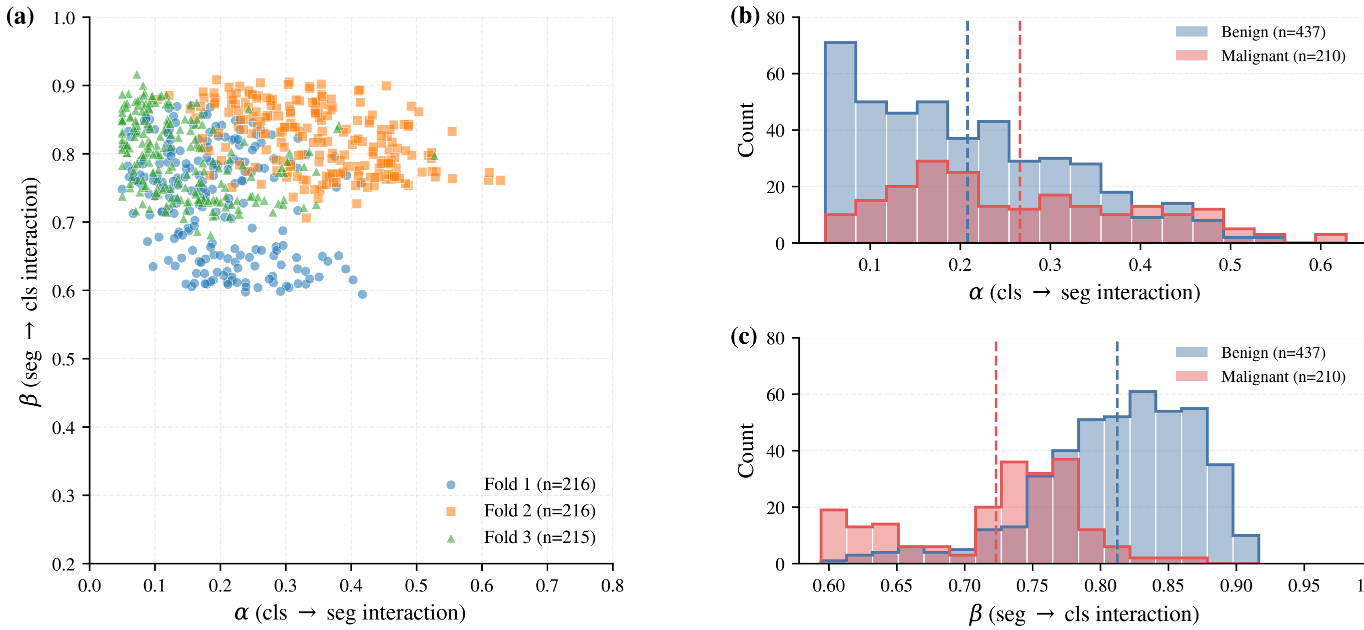

Fig. 5: Visualization of learned bidirectional gating coefficients α and β across all 647 test samples from three cross-validation folds on the BUSI dataset. (a) Scatter plot of sample-wise α and β values, with different colors and markers denoting cross-validation folds. (b, c) Class-wise distributions of α and β, grouped by ground-truth labels, with dashed vertical lines indicating class-specific means. The dispersion of points in (a) confirms that gating coefficients vary adaptively across samples rather than collapsing to fixed values. Furthermore, (b) and (c) reveal class-dependent patterns: benign cases exhibit lower α and higher β values compared to malignant cases, indicating that the gating mechanism learns meaningful, feature-driven adaptations rather than random assignments.

22.56M parameters, and an inference speed of 64.10 FPS. The additional computation introduced by TSFE-ITFI is primarily dedicated to decoder-side contextual refinement and explicit bidirectional task interaction, thereby enhancing lesion-aware feature representations more effectively. It is worth noting that compared with CTEF-UNet, TSFE-ITFI substantially reduces the parameter count from 75.86M to 22.56M while maintaining comparable inference speed. Although its FLOPs increase slightly, this minor overhead is offset by consistent gains across all evaluation metrics. These results demonstrate that TSFE-ITFI achieves a superior trade-off between computational complexity and joint segmentation-classification performance compared to representative competing methods.

6. Conclusion

In this paper, we present TSFE-ITFI, a unified framework for joint breast tumor segmentation and classification in BUS images. By integrating the Task-Specific Feature Enhancement (TSFE) strategy and the Inter-Task Feature Interaction (ITFI) mechanism, the proposed framework improves task-specific representations while promoting effective collaboration between segmentation and classification. In particular, the Convolution-Mamba2 feature fusion (CM2FF) block strengthens contextual modeling and local detail preservation in the segmentation branch, while the multi-scale channel-spatial attention (MSCSA) mechanism facilitates robust feature extraction in the classification branch, and the bidirectional task interaction (BTI) module enables adaptive bidirectional feature exchange between segmentation and classification. Experimental results on two public BUS datasets demonstrate that TSFE-ITFI achieves robust and competitive performance in both tasks, indicating its potential as an effective framework for computer-aided breast ultrasound analysis.

Nevertheless, several limitations should be acknowledged. The current study is validated only on two publicly available BUS datasets, and further evaluation on larger multi-source datasets is still required to assess its generalizability in real-world clinical settings. In addition, the robustness analysis is conducted only on the BUSI dataset using synthetic perturbations. Therefore, the current results provide preliminary evidence of classification stability under the evaluated synthetic perturbations, but not real-world clinical robustness. Moreover, the proposed framework is currently limited to lesion segmentation and benign-malignant discrimination, and its utility for broader ultrasound diagnostic scenarios requires further investigation. Therefore, future work will focus on multi-source validation, model simplification and optimization, extension to a wider range of breast ultrasound analysis tasks, and exploration of its potential applicability to other medical imaging modalities.

Data availability statement

All data that support the findings of this study are included within the article (and any supplementary information files).

CRediT authorship contribution statement

Libin Lan: Conceptualization, Funding Acquisition, Methodology, Project Administration, Software, Writing – Original Draft Preparation, Writing – Review & Editing.

Minghui Li: Data Curation, Investigation, Methodology, Software, Writing – Original Draft Preparation, Visualization, Writing – Review & Editing.

Declaration of competing interest

The authors declare that they have no known competing financial interests or personal relationships that could have appeared to influence the work reported in this paper.

Acknowledgments

This work described in this paper was supported in part by the Scientific Research Foundation of Chongqing University of Technology under Grant 2021ZDZ030 and in part by the Youth Project of Science and Technology Research Program of Chongqing Education Commission of China under Grant KJQN202301145.

References

[1] F. Bray, M. Laversanne, H. Sung, et al., Global cancer statistics 2022: Globocan estimates of incidence and mortality worldwide for 36 cancers in 185 countries, CA: a cancer journal for clinicians 74 (3) (2024) 229–263.

[2] M. Bahl, J. M. Chang, L. A. Mullen, et al., Artificial intelligence for breast ultrasound: Ajr expert panel narrative review, American Journal of Roentgenology 223 (6) (2024) e2330645.

[3] Q. He, Q. Yang, H. Su, et al., Multi-task learning for segmentation and classification of breast tumors from ultrasound images, Computers in Biology and Medicine 173 (2024) 108319.

[4] Z. Fan, P. Gong, S. Tang, et al., Joint localization and classification of breast masses on ultrasound images using an auxiliary attention-based framework, Medical image analysis 90 (2023) 102960.

[5] A. Vaswani, N. Shazeer, N. Parmar, et al., Attention is all you need, in: Advances in Neural Information Processing Systems, Vol. 30, 2017.

[6] A. Gu, T. Dao, Mamba: Linear-time sequence modeling with selective state spaces, in: First Conference on Language Modeling, 2024.

[7] T. Dao, A. Gu, Transformers are SSMs: Generalized models and efficient algorithms through structured state space duality, in: Proceedings of the 41st International Conference on Machine Learning, Vol. 235, PMLR, 2024, pp. 10041–10071.

[8] O. Ronneberger, P. Fischer, T. Brox, U-net: Convolutional networks for biomedical image segmentation, in: International Conference on Medical image computing and computer-assisted intervention, Springer, 2015, pp. 234–241.

[9] O. Oktay, J. Schlemper, L. Le Folgoc, et al., Attention U-Net: Learning where to look for the pancreas, in: Proceedings of the 1st Conference on Medical Imaging with Deep Learning (MIDL), 2018.

[10] Z. Zhou, M. M. Rahman Siddiquee, N. Tajbakhsh, et al., Unet++: A nested u-net architecture for medical image segmentation, in: International workshop on deep learning in medical image analysis, Springer, 2018, pp. 3–11.

[11] L.-C. Chen, Y. Zhu, G. Papandreou, et al., Encoder-decoder with atrous separable convolution for semantic image segmentation, in: Proceedings of the European conference on computer vision (ECCV), 2018, pp. 801–818.

[12] S. Feng, H. Zhao, F. Shi, et al., CPFNet: Context pyramid fusion network for medical image segmentation, IEEE transactions on medical imaging 39 (10) (2020) 3008–3018.

[13] C. Xue, L. Zhu, H. Fu, et al., Global guidance network for breast lesion segmentation in ultrasound images, Medical image analysis 70 (2021) 101989.

[14] G. Chen, L. Li, Y. Dai, et al., Aau-net: an adaptive attention u-net for breast lesions segmentation in ultrasound images, IEEE Transactions on Medical Imaging 42 (5) (2022) 1289–1300.

[15] G. Chen, Y. Dai, J. Zhang, C-Net: Cascaded convolutional neural network with global guidance and refinement residuals for breast ultrasound images segmentation, Computer Methods and Programs in Biomedicine 225 (2022) 107086.

[16] H. Zhang, J. Lian, Z. Yi, et al., HAU-Net: Hybrid cnn-transformer for breast ultrasound image segmentation, Biomedical Signal Processing and Control 87 (2024) 105427.

[17] M. A. G. Nadeem Zaidkilani, D. Puig, CoAtUNet: A symmetric encoder-decoder with hybrid transformers for semantic segmentation of breast ultrasound images, Neurocomputing 629 (2025) 129660.

[18] Y. Lyu, Y. Xu, X. Jiang, et al., AMS-PAN: Breast ultrasound image segmentation model combining attention mechanism and multi-scale features, Biomedical Signal Processing and Control 81 (2023) 104425.

[19] J. Huang, Y. Mao, J. Deng, et al., EMGANet: Edge-aware multi-scale group-mix attention network for breast cancer ultrasound image segmentation, IEEE Journal of Biomedical and Health Informatics 29 (8) (2025) 5631–5641.

[20] D. Sun, C. Dong, Y. Yan, et al., Challenge-aware u-net for breast lesion segmentation in ultrasound images, Pattern Recognition 168 (2025) 111851.

[21] X. H. Yangyang Li, Xintong Hou, et al., Bilateral-aware and multi-scale region guided u-net for precise breast lesion segmentation in ultrasound images, Neurocomputing 632 (2025) 129775.

[22] J. Ma, F. Li, B. Wang, U-mamba: Enhancing long-range dependency for biomedical image segmentation, arXiv preprint arXiv:2401.04722 (2024).

[23] J. Ruan, J. Li, S. Xiang, Vm-unet: Vision mamba unet for medical image segmentation, ACM Transactions on Multimedia Computing, Communications and Applications (2024).

[24] T. Fujioka, M. Mori, K. Kubota, et al., The utility of deep learning in breast ultrasonic imaging: a review, Diagnostics 10 (12) (2020) 1055.

[25] Y. Wang, E. J. Choi, Y. Choi, et al., Breast cancer classification in automated breast ultrasound using multiview convolutional neural network with transfer learning, Ultrasound in medicine & biology 46 (5) (2020) 1119–1132.

[26] A. AlZoubi, F. Lu, Y. Zhu, et al., Classification of breast lesions in ultrasound images using deep convolutional neural networks: transfer learning versus automatic architecture design, Medical & Biological Engineering & Computing 62 (1) (2024) 135–149.

[27] M. Byra, K. Dobruch-Sobczak, H. Piotrzkowska-Wroblewska, et al., Explaining a deep learning based breast ultrasound image classifier with saliency maps, Journal of Ultrasonography 22 (89) (2022) 70.

[28] Y. Luo, Q. Huang, X. Li, Segmentation information with attention integration for classification of breast tumor in ultrasound image, Pattern Recognition 124 (2022) 108427.

[29] M. Varol Arısoy, Edge-refined cross-task multi-level dense fusion for accurate breast ultrasound segmentation and classification, Neurocomputing 658 (2025) 131793.

[30] R. Caruana, Multitask learning, Machine learning 28 (1) (1997) 41–75.

[31] A. Kendall, Y. Gal, R. Cipolla, Multi-task learning using uncertainty to weigh losses for scene geometry and semantics, in: Proceedings of the IEEE conference on computer vision and pattern recognition, 2018, pp. 7482–7491.

[32] Z. Chen, V. Badrinarayanan, C.-Y. Lee, et al., Gradnorm: Gradient normalization for adaptive loss balancing in deep multitask networks, in: International conference on machine learning, PMLR, 2018, pp. 794–803.

[33] K. Ren, K. Zou, X. Liu, et al., Uncertainty-informed mutual learning for joint medical image classification and segmentation, in: International Conference on Medical Image Computing and Computer-Assisted Intervention, Springer, 2023, pp. 35–45.

[34] S. Liu, E. Johns, A. J. Davison, End-to-end multi-task learning with attention, in: Proceedings of the IEEE/CVF conference on computer vision and pattern recognition, 2019, pp. 1871–1880.

[35] Y. Ling, Y. Wang, W. Dai, et al., MTANet: Multi-task attention network for automatic medical image segmentation and classification, IEEE Transactions on Medical Imaging 43 (2) (2024) 674–685.

[36] S. Woo, J. Park, J.-Y. Lee, et al., CBAM: Convolutional block attention module, in: Proceedings of the European conference on computer vision (ECCV), 2018, pp. 3–19.

[37] J. Hu, L. Shen, G. Sun, Squeeze-and-excitation networks, in: Proceedings of the IEEE conference on computer vision and pattern recognition, 2018, pp. 7132–7141.

[38] A. Gu, K. Goel, C. Ré, Efficiently modeling long sequences with structured state spaces, in: International Conference on Learning Representations (ICLR), 2022.

[39] B. Lin, W. Jiang, P. Chen, et al., MTMamba: Enhancing multi-task dense scene understanding by mamba-based decoders, in: European conference on computer vision, Springer, 2024, pp. 314–330.

[40] K. He, X. Zhang, S. Ren, et al., Deep residual learning for image recognition, in: Proceedings of the IEEE conference on computer vision and pattern recognition, 2016, pp. 770–778.

[41] Y. Wu, K. He, Group normalization, in: Proceedings of the European conference on computer vision (ECCV), 2018, pp. 3–19.

[42] R. Zhang, M. Xie, A multi-task learning model with low-level feature sharing and inter-feature guidance for segmentation and classification of medical images, in: 2024 IEEE International Conference on Bioinformatics and Biomedicine (BIBM), IEEE, 2024, pp. 2894–2899.

[43] J. Wei, S. Wang, Q. Huang, F^3Net: fusion, feedback and focus for salient object detection, in: Proceedings of the AAAI conference on artificial intelligence, Vol. 34, 2020, pp. 12321–12328.

[44] X. Zhao, L. Zhang, H. Lu, Automatic polyp segmentation via multi-scale subtraction network, in: International Conference on Medical Image Computing and Computer-Assisted Intervention, Springer, 2021, pp. 120–130.

[45] W. Al-Dhabyani, M. Gomaa, H. Khaled, et al., Dataset of breast ultrasound images, Data in brief 28 (2020) 104863.

[46] F. Isensee, P. F. Jaeger, S. A. Kohl, et al., nnu-net: a self-configuring method for deep learning-based biomedical image segmentation, Nature methods 18 (2) (2021) 203–211.

[47] J. Chen, Y. Lu, Q. Yu, et al., Transunet: Transformers make strong encoders for medical image segmentation, arXiv preprint arXiv:2102.04306 (2021).

[48] Y. Yue, Z. Li, Medmamba: Vision mamba for medical image classification, arXiv preprint arXiv:2403.03849 (2024).

[49] C. Chen, W. Bai, D. Rueckert, Multi-task learning for left atrial segmentation on ge-mri, in: International workshop on statistical atlases and computational models of the heart, Springer, 2018, pp. 292–301.

[50] Y. Zhang, Y. Sun, H. Li, S. Zheng, C. Zhu, L. Yang, Benchmarking the robustness of deep neural networks to common corruptions in digital pathology, in: L. Wang, Q. Dou, P. T. Fletcher, S. Speidel, S. Li (Eds.), Medical Image Computing and Computer Assisted Intervention – MICCAI 2022, Springer Nature Switzerland, Cham, 2022, pp. 242–252.